Energy 342 (2026) 139726

Contents lists available at ScienceDirect

Energy

journal homepage: www.elsevier.com/locate/energy

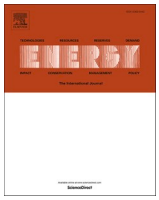

Experimental and numerical investigation of the fire behavior of double-glass building integrated photovoltaic modules with PVB interlayers

Wanning Yu [a,b], Lizhong Yang [a], Xinyang Wang [a], Dimeng Lai [c], Grunde Jomaas [d], K.M. Liew [b,*], Xiaoyu Ju [a,**]

[a] State Key Laboratory of Fire Science, University of Science and Technology of China, Hefei, China
[b] Department of Architecture and Civil Engineering, City University of Hong Kong, Hong Kong SAR, China
[c] School of Marine Equipment and Mechanical Engineering, Jimei University, Xiamen, China
[d] FRISSBE, Slovenian National Building and Civil Engineering Institute (ZAG), Ljubljana, Slovenia

ARTICLE INFO

Keywords:
Building-integrated photovoltaics (BIPV)
Fire performance
Double-glass photovoltaic modules
Thermal degradation
Toxic gas emissions

ABSTRACT

Amid rising global energy demands and environmental concerns, energy-efficient, or 'green', buildings are becoming mandatory in building regulations worldwide. In that context, building-integrated photovoltaics (BIPV), which merge photovoltaic (PV) modules with architectural design, are gaining widespread adoption. To assess fire safety aspects of BIPV, the fire performance of double-glass PV modules with polyvinyl butyral (PVB) encapsulation in BIPV façade systems was studied experimentally and numerically. More specifically, fire experiments were conducted under varying radiative heat fluxes to evaluate thermal degradation, fire behavior, and toxic gas emissions. Key parameters, including ignition time, heat release rate per unit area (HRRPUA), mass loss rate (MLR), and gas composition, were analyzed. The results confirm that a higher external heat flux markedly reduces ignition time while increasing HRRPUA and MLR for BIPV, which is in line with results for other materials. The primary toxic gases emitted during combustion were CO, CO_2, H_2, and SO_2, with CO and CO_2 emissions rising significantly at elevated heat fluxes. To complement the experimental results, a numerical model coupling transient heat conduction and pyrolysis kinetics was developed to predict the pre-ignition thermal response of the multilayer structure. The model employed layer discretization and temperature-dependent boundaries, demonstrating close agreement with experimental data. Therefore, it enabled systematic analyses of the sensitivity of PV module material flammability to incident radiative heat fluxes, material properties, and geometric configurations. This combined experimental and numerical approach offers a predictive framework for assessing fire risks and optimizing the fire safety design of BIPV systems.

1. Introduction

With increasing global energy demand and growing environmental concerns, energy-efficient or "green" buildings have emerged as a necessity in construction [1–4]. Countries worldwide are accelerating their carbon-peaking and carbon-neutrality commitments, spurring the rapid deployment of green-building practices. Building-integrated photovoltaics (BIPV), which incorporate photovoltaic (PV) modules into façades, roofs, and other architectural components, present a sustainable solution for clean energy generation and reduced overall energy consumption [5–7]. PV façades, in particular, combine energy production with thermal insulation, aesthetic appeal, and fire resistance, driving their widespread adoption in modern architecture.

Buildings have diverse requirements for PV modules. Double-glass PV modules, commonly used in BIPV curtain wall systems, typically consist of front and rear glass panes, PV cells, and combustible interlayers. Unlike traditional cover-glass or polyethylene terephthalate (PET)-laminated PV modules (Fig. 1), double-glass structures (Fig. 2) provide superior aesthetics, transparency, and structural strength [8–10]. These modules are often installed vertically on building façades to enhance mechanical stability [11,12]. However, since this material contains organic components, it inherently possesses potential combustibility and will undergo pyrolysis and release toxic gases during a fire [13,51,52]. A thorough investigation of their thermal degradation

* Corresponding author.
** Corresponding author.
E-mail addresses: kmliew@cityu.edu.hk (K.M. Liew), ju.xiaoyu@ustc.edu.cn (X. Ju).

https://doi.org/10.1016/j.energy.2025.139726
Received 4 September 2025; Received in revised form 26 November 2025; Accepted 17 December 2025
Available online 20 December 2025

processes and toxic emission characteristics is therefore essential.

Numerous studies have investigated the thermal and toxicological properties of PV modules under varying conditions. Chow et al. [14] analyzed cover-glass PV modules and modules with polyurethane and epoxy encapsulants exposed to 10–70 kW/m^2 radiant heat fluxes, including characterizing chemical changes via FTIR and XPS. Yang et al. [15] and Ju et al. [16] employed cone calorimetry to examine EVA-based modules with glass/PET outer layers to evaluate ignition behavior, mass loss rate, heat release, and CO/CO_2 emissions. Expanding on this work, Liao et al. [17] conducted bench-scale tests on medium-sized PET-laminated PV modules, identifying toxic emissions including SO_2, HF, HCN, and VOCs. Wang et al. [18] used a fire propagation apparatus to compare cover- and double-glass EVA-laminated modules, demonstrating higher flammability in cover-glass module backsheets. While these studies employed stable atmospheric conditions, Liao et al. [19] later demonstrated that increased airflow and external radiation elevate fire risks in PET modules. Xu et al. [20] further investigated cover-glass PV modules at 60–100 kPa ambient pressure, establishing correlations between flame height, radiation intensity, and air pressure.

Most previous research has focused on cover-glass and PET-laminated PV modules, primarily for ground-mounted [17,19,21,22] and rooftop [5,16,20,23] PV systems, offering key insights into their thermal and fire behavior. However, the rapid advancement of BIPV technologies has led to widespread adoption of double-glass modules in façade applications. Their extensive surface area raises new fire safety challenges, particularly in high-rise and densely built environments. Recent studies have begun addressing fire and smoke behavior in BIPV curtain walls: Qi et al. [24–26] employed helium as a smoke surrogate to analyze smoke movement using particle image velocimetry (PIV) and computational fluid dynamics (CFD), circumventing the safety and cost constraints of full-scale fire experiments. Miao and Chow [27] investigated PV model combustion effects by constructing an 8-m-high shaft connected to a test chamber under room fire conditions. Stølen et al. [28] evaluated thermal failure through SP FIRE 105 façade testing on a full-scale curtain wall incorporating 26 PV modules. Although these studies have explored certain aspects of fire and smoke behavior in BIPV curtain walls, systematic investigation into the pyrolysis, combustion, and emission characteristics of double-glass BIPV modules remains limited.

In this work, this research gap is addressed through a systematic investigation of the fire behavior of double-glass PV modules with PVB encapsulation in BIPV façades. Ignition experiments were performed under different radiative heat fluxes to measure ignition time, heat release rate per unit area (HRRPUA), mass loss rate (MLR), and toxic gas emissions from the modules. Complementing the experimental work, based on experimental data, a numerical model was developed for simulating pre-ignition thermal response and pyrolysis processes in the multilayer structure under radiative heat flux. The model integrates transient heat conduction with pyrolysis kinetics, employing a layer-wise discretization method to accurately predict internal temperature distribution. By combining experimental and computational approaches, this work offers a robust framework for evaluating fire performance in BIPV applications.

2. Materials and methods

2.1. Sample

The PV modules used in this study are double-glass with a five-layer structure (as shown in Fig. 2). The front panel is made of ordinary clear glass, and the back panel is made of ultra-white glass. A crystalline silicon PV cell is sandwiched between two layers of PVB encapsulant. To preserve the mechanical and combustion integrity of the module and to enhance the representativeness of the experimental results, the width and height of the test specimens were selected as 300 mm × 300 mm. Each glass layer has a thickness of 6 mm, while each PVB layer is 0.8 mm thick, resulting in a total module thickness of 13.7 ± 0.3 mm. All specimens were manufactured by Baoding Jiasheng Photovoltaic Technology Co., Ltd. The sample mass was 3000.0 ± 20.0 g. The detailed thermophysical properties of each layer in the PV module are listed in Table 1.

2.2. Experimental setup

The fire experiments were conducted using the early-stage fire

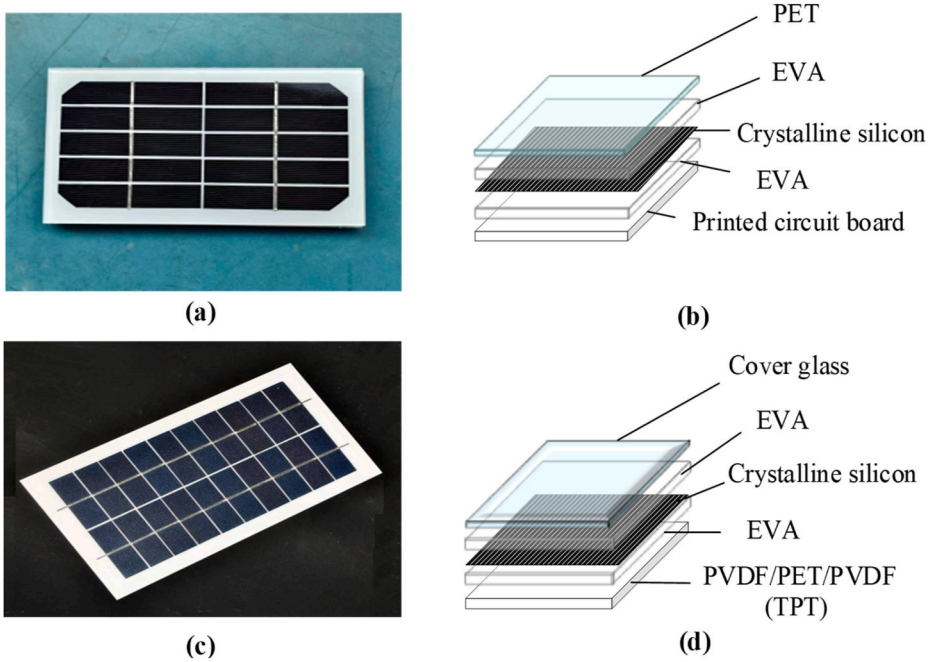

Fig. 1. PET-laminated PV module: (a) Photograph of the physical item, (b) Decomposed view of the elements and cover-glass; PV module: (c) Photograph of the physical item, (d) Decomposed view of the elements.

characteristics bench at the State Key Laboratory of Fire Science, a facility developed with reference to ISO 5660 [17]. The radiant heat source of the platform has a dimension of 500 mm × 600 mm, which allows for the testing of medium to large sized materials such as those used in this study.

As shown in Fig. 3, the test platform was enclosed in a glass ventilation hood. At the bottom, an adjustable platform supported an electronic balance, which was protected by a ceramic fiber board placed between it and the test sample. A panel of silicon carbide rods served as the radiant heat source mounted atop the platform, and an exhaust hood above it was connected to an exhaust duct.

By adjusting the power input to the silicon carbide heating elements, irradiance levels were set to 20, 25, 30, 35, and 40 kW/m^2 [16,29,30]. Prior to each test, the heat flux was calibrated using a radiative heat flux meter. All experiments were conducted under ambient air conditions and mass loss was monitored in real time using an electronic balance with an accuracy of 0.1 g. The exhaust duct was connected to a Servomex 4100 gas analyzer, which was used to continuously measure concentrations of multiple gases, including CO, CO_2, H_2, and SO_2.

To ensure vertical radiant heating from the top heat source, the bottom and sides of each specimen were covered with aluminum foil during testing. Preliminary tests were conducted on both the front and rear glass panels of the double-glass PV modules under radiative heating, revealing no significant difference in combustion behavior. Therefore, no distinction was made between front and rear panels during formal testing.

2.3. Numerical prediction model of inner layer temperature of double-glass PV modules

Fire tests of PV curtain walls are resource-intensive, and numerous parameters are hard to measure, with the overall dynamic evolution of the temperature field being especially difficult to predict. Therefore, a numerical model capable of accurately predicting the pre-ignition thermal response and pyrolysis behavior of double-glass PV modules is essential. Such a model enables in-depth analysis of temperature evolution and material degradation in multilayer structures, as well as sensitivity studies on key parameters including incident radiative heat flux, material properties, and module configuration. When validated against limited experimental data, the model provides an efficient and economical approach for evaluating fire performance, optimizing encapsulation materials, and guiding fire-safety design of double-glass PV façades.

The overall workflow of the numerical modeling process is illustrated in Fig. 4. The following sections provide detailed descriptions of main steps.

2.3.1. Governing equations

The numerical prediction model was developed based on a one-dimensional transient heat conduction model, which is derived from the energy and mass conservation equations. It incorporates the pyrolysis kinetics of the PVB interlayer, described by the Arrhenius equation, and couple density variations induced by pyrolysis to the governing heat transfer equations.

Table 1
Thermophysical properties of the double-glass PV interlayers.

Properties	Layer Name		
	Glass	Silicon Cell	PVB
Specific Heat Capacity (J/kg·K)	890	985	2780
Thermal Conductivity (W/m·K)	1.03	1.33	0.23
Density (kg/m^3)	800	2250	2500

Considering that PV modules function as photo-thermal conversion devices, their energy conversion efficiency is closely related to optical transmittance characteristics. Both the glass cover and the PVB interlayer are transparent materials whose spectrally selective transmission significantly influences the effective transport path of incident photons and interfacial reflection losses. Therefore, in-depth absorption assumption was adopted in the numerical model [31–33], in which the incident radiative heat flux is gradually absorbed and exponentially attenuates with depth in the material (in Fig. 5). In Fig. 5, I_0 denotes the total incident radiation intensity on the material surface, while r represents the reflectivity of the material with respect to the incident radiation. Accordingly, the differential equation for the transient heat-conduction process can be expressed as Eq. (1):

$$\frac{\partial \theta}{\partial t} = \alpha \frac{\partial^2 \theta}{\partial x^2} + \dot{q}''_{ext} \kappa e^{-\kappa x} \tag{1}$$

In this equation, $\theta = T(x,t) - T_i$ represents the temperature rise relative to the initial temperature T_i; t is the time coordinate; α represents the thermal diffusivity, $\dot{q}''_{ext}$ denotes the external radiant heat flux, and κ is the depth-dependent absorption coefficient.

2.3.2. Initial and boundary conditions

The thermal model is developed based on a one-dimensional assumption, with Neumann-type adiabatic boundary conditions imposed along the radial and bottom boundaries [34]. To enhance computational efficiency and ensure clear coupling of the underlying physical mechanisms, several key simplifications are introduced. For greater clarity and transparency, the main assumptions of the numerical model are summarized in Table 2.

The 1D model cannot capture lateral heat transfer or local temperature variations, and may underestimate the influence of structural changes such as bubble formation and multiphase flow coupling. However, it is computationally efficient and provides reliable predictions of through-thickness thermal response, making it suitable for preliminary analysis and material optimization.

The initial and boundary conditions of the model are as follows:

$$\theta(x,0) = 0 \tag{2}$$

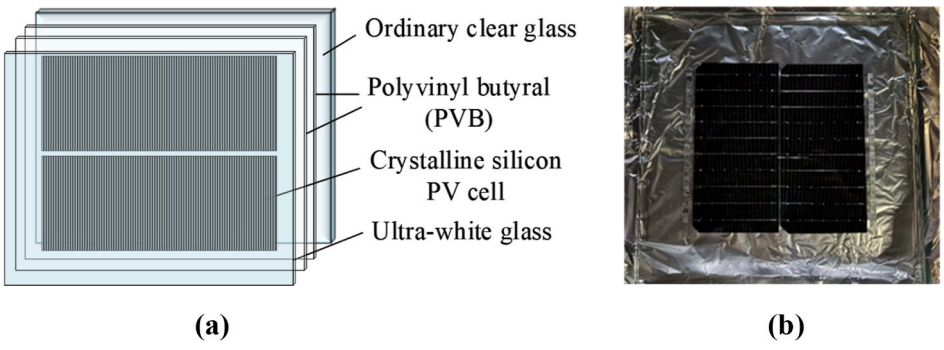

Fig. 2. Double-glass PV module. (a) Decomposed view of the elements and (b) Photograph of the physical item (300 mm × 300 mm).

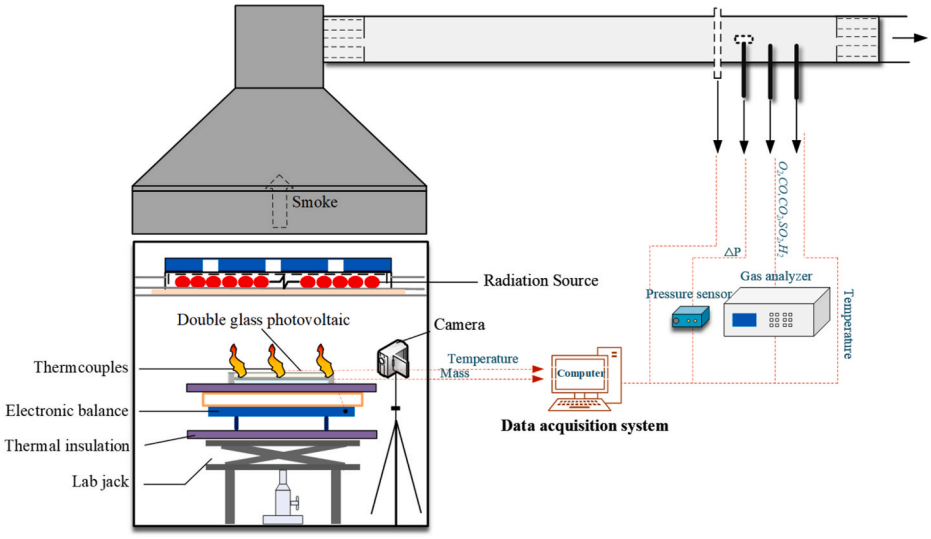

Fig. 3. Schematic of early-stage experimental setup.

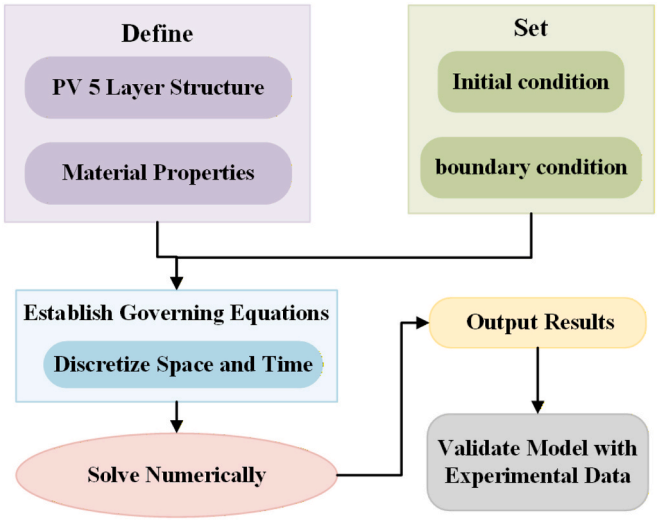

Fig. 4. Workflow diagram of the numerical modeling process.

$$\theta(\infty, t) = 0 \tag{3}$$

$$-k\frac{\partial\theta}{\partial x}|_{x=0} = -h_c\theta - \varepsilon\sigma\left(T^4 - T_i^4\right) \tag{4}$$

Here, x denotes the radial spatial coordinate; h_c is the convective heat transfer coefficient; ε is the surface emissivity, $\varepsilon = 0.8$; σ is the Stefan-Boltzmann constant, $\sigma = 5.67 \times 10^{-8}$ W/m^2·K^4.

2.3.3. *Layer-wise discretization method*

A previous study [21] simulated the pre-ignition temperature field of multilayer non-homogeneous materials by treating the layers as a single composite using a cumulative thickness approach. However, this method overlooks the distinct thermal behaviors of individual layers due to differences in their physical properties. In contrast, a layer-wise discretization method is applied here for spatial discretization, establishing separate governing equations for the five-layer structure (glass--PVB-silicon-PVB-glass). Each material layer is assigned independently

Table 2
Key assumptions of the numerical model.

No.	Assumption
1	The initial temperature of the module is uniform and the lateral heat transfer is neglected
2	Geometric deformations caused by phase transitions are neglected
3	Pyrolysis products are assumed to undergo instantaneous gas-solid separation upon formation

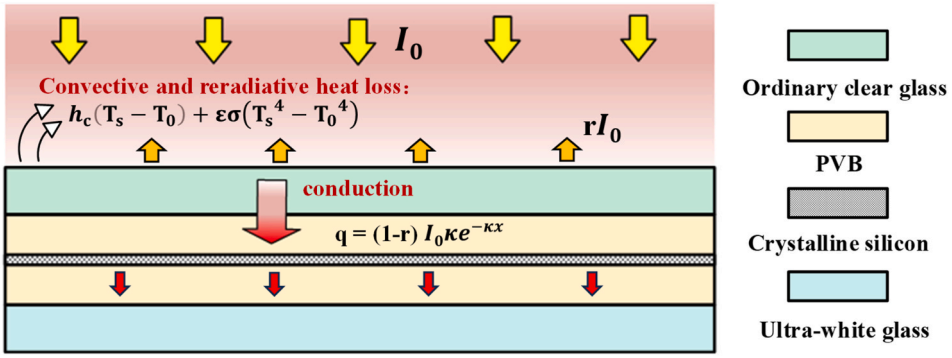

Fig. 5. Heat transfer process in the double-glass PV modules.

defined thermal properties, including thermal conductivity, specific heat capacity, and density. To ensure continuous heat flux at the interfaces, the thermal conductivity between dissimilar materials is treated using the harmonic mean method, accurately capturing temperature gradients during interlayer heat transfer.

$$K_a = \frac{2k_i k_j}{k_i + k_j} \tag{5}$$

In the governing equations, k_i and k_j denote the equivalent thermal conductivities at material interfaces.

The spatial discretization was performed using the finite volume method with a spatial step size of 1 mm, while temporal discretization was carried out using an explicit iterative algorithm to resolve the temperature field evolution over time. This approach accurately captures the temperature gradients and thermal barriers in the multilayer structure, thereby preventing smoothing errors in the temperature field associated with discontinuities of thermal conductivity across material interfaces.

3. Results and discussions

3.1. Experimental phenomena

Several noteworthy phenomena were observed during the fire tests, based on which the pyrolysis process of the double-glass PV modules were divided into six distinct stages: preheating, gasification, edge burning, complete combustion, decay, and cooling (in Fig. 6). The modules were placed horizontally, exposed to heat flux from above, and the process was recorded using a camera with a resolution of 1920 × 1080 pixels and a frame rate of 25 frames per second.

Initially, sustained thermal radiation, the surface temperature of the PV module increased gradually, exhibiting a typical top-down heat transfer pattern (preheating stage). As the temperature of the panel surface continued to rise, and the encapsulated PVB began to melt once the inner layer temperature approached approximately 165 °C. The molten PVB started to flow from the edges of the module, seeping into the aluminum foil, and forming bubbles. These bubbles expanded and collapsed rapidly, releasing a large volume of white, smoke-like vapor. As the vapor concentration rose, ignition occurred near the heat source once a flammable mixture formed, and flames rapidly spread along the module edges. Due to the glass layers enclosing the front and back surfaces, the flame propagation was largely restricted to the edges of the modules, which was defined as the edge burning stage.

As combustion progressed, flames spread along the module's perimeter, causing a temperature gradient between the edges and the center of the glass surface. This gradient led to the accumulation of thermal stress, eventually exceeding the structural limit of the glass. The result was a sudden, explosive fracture accompanied by a loud cracking sound, with sharp glass fragments projected outwards. The expanding cracks facilitated flame intrusion into the encapsulated interior layers, igniting the remaining PVB and causing the entire surface to be engulfed in flames. This phase is defined as the complete combustion stage.

As the internal PVB material was gradually consumed, the flame intensity diminished, indicating the beginning of the decay stage, during which the flames reduced in size and eventually extinguished. With the disappearance of the flame, the thermal feedback to the material ceased, resulting in a rapid temperature drop. This change triggered further glass breakage, resulting in needle-like and jagged shards, as shown in Fig. 7.

Notably, glass fracture was observed not only during the intense burning phase but also, and more frequently, during the cooling stage, primarily as a result of thermal shock. In real fire scenarios, this suggests that the gasification, complete combustion, and cooling stages all pose significant safety hazards, including the dripping of molten PVB and fragmentation of glass, which may result in falling debris hazards for building façades and high-rise structures.

It should be emphasized that this study used unsealed-edge samples to reveal the fundamental fire behavior of double-glass PV modules. In

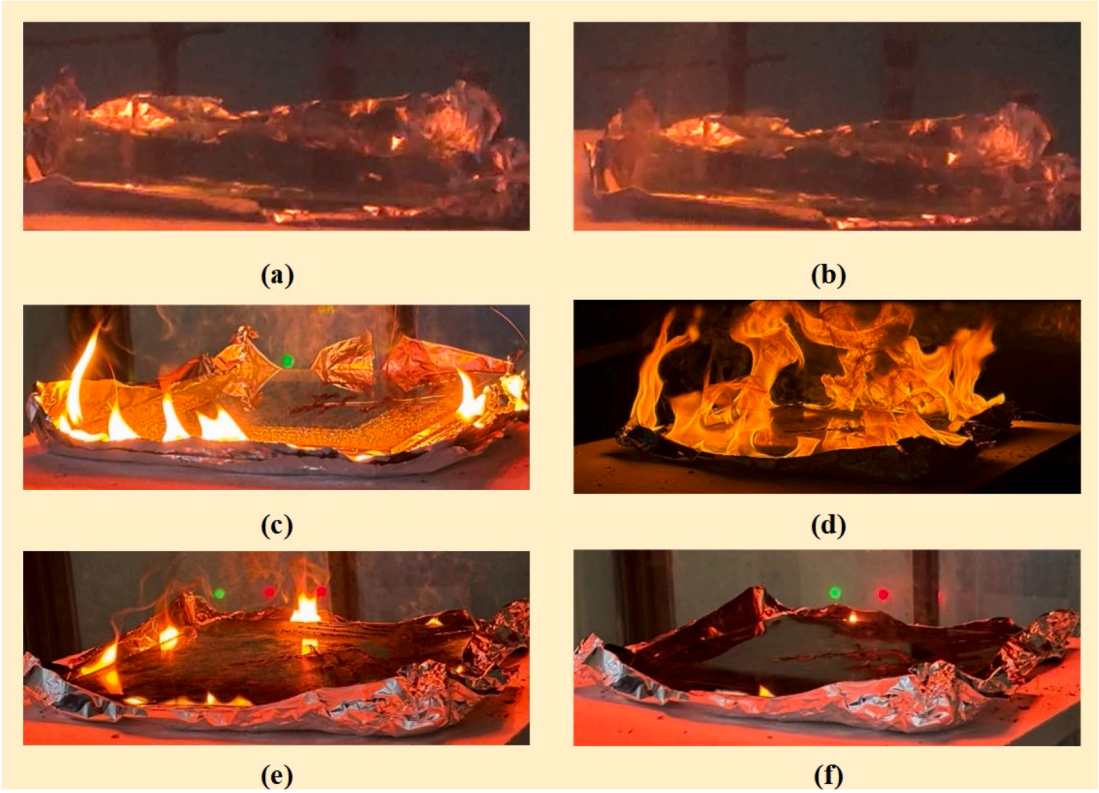

Fig. 6. Pyrolysis process: (a) Preheating, (b) Gasification, (c) Edge burning, (d) Complete combustion, (e) Decay, (f) Cooling.

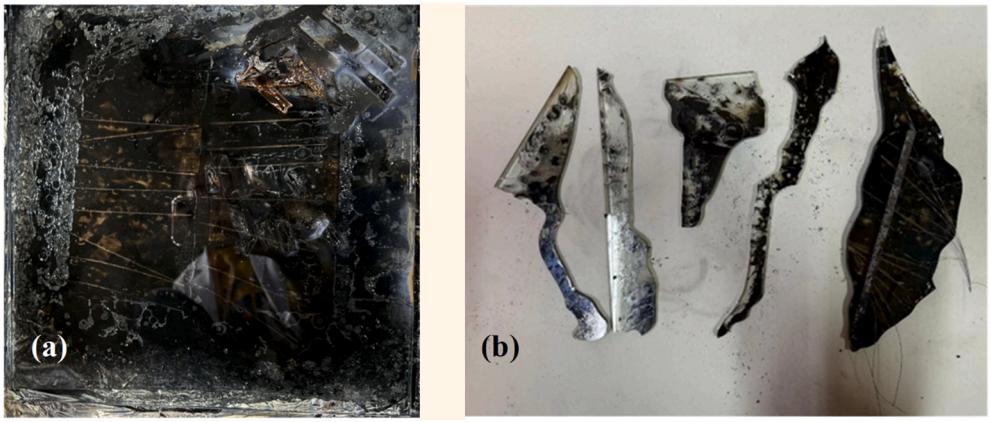

Fig. 7. Combustion residues: (a) post-combustion double-glass PV module (300 mm × 300 mm); (b) glass shards generated from module fracture.

practice, most BIPV modules are sealed or framed, which may delay PVB outflow, extend ignition time, and introduce additional combustible materials. Moreover, real-world modules undergo environmental aging, such as UV exposure and moisture. These factors may change the properties of the encapsulant and seals, and thus affect fire behavior. Therefore, further research is needed to evaluate how edge treatments and aging impact fire performance.

3.2. Ignition behavior

Ignition time, as a key indicator of pyrolysis and fire hazard, was defined in this study as the time interval from the exposure of the PV module under the radiative heating source to the moment of sustained ignition. The results under different irradiance levels are shown in Fig. 8. Specifically, the average ignition time at 20 kW/m^2 was 461 s, while at 40 kW/m^2 it dropped to 118 s, a difference of almost 6 min.

A comparison was made with previously reported ignition times for PET-laminated PV modules [17] and cover-glass PV modules [15]. As shown in Fig. 8, under equivalent heat flux conditions, the ignition times followed the order: Cover-glass PV > Double-glass PV > PET-laminated PV. From the perspective of flame spread and fire safety, this suggests that while double-glass PV modules offer superior light transmittance, their resistance to initial fire exposure is lower than that of cover-glass PV modules but higher than that of PET-laminated ones.

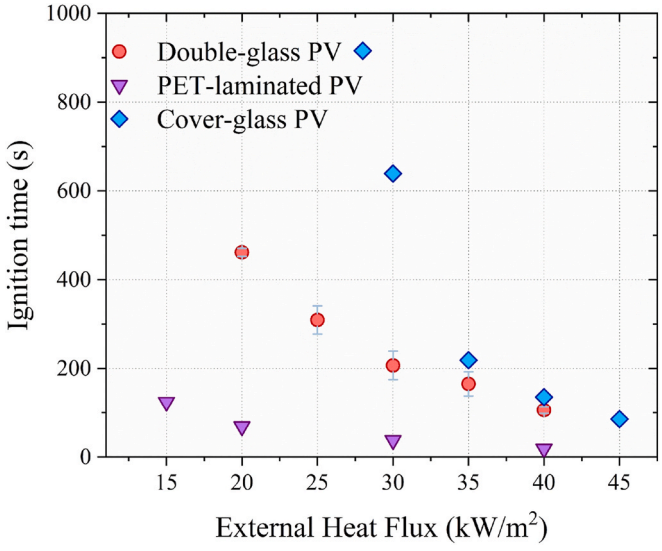

Fig. 8. Ignition times of double-glass PV, cover-glass PV [15], and PET-laminated PV [17].

In thermal models for solid ignition, combustible solids are typically classified as thermally-thick or thermally-thin. For multilayer composites such as PV modules, the thermal-thick or thermal-thin behavior cannot be determined by a single effective thermal conductivity or penetration depth due to the distinct properties of each layer. Instead, two main approaches are used: fitting the ignition time and external heat flux data with a power-law relationship, and directly measuring temperature distribution during heating. The former provides an overall indication of thermal response, while the latter identifies thermal-thick behavior by a clear temperature gradient or thermal-thin behavior by a uniform profile [35,36]. Together, these methods offer a comprehensive evaluation of multilayer materials thermal characteristics.

According to the work of Quintiere et al. [37–39], for thermally-thick materials, the relationship between ignition time, ignition temperature, and external heat flux follows Equations (6) and (7), in which the square root of the reciprocal of the ignition time is linearly correlated with heat flux. For thermally-thin materials, the relationship takes a different form, where the reciprocal of ignition time is linearly related to the heat flux.

$$t_{ig} \approx \frac{\pi}{4} k\rho c \left(\frac{T_{ig} - T_\infty}{\dot{q}_e^{''}} \right)^2 \tag{6}$$

$$\sqrt{\frac{1}{t_{ig}}} = \frac{\sqrt{4/\pi(\dot{q}_e^{''} - \mathrm{CHF})}}{k\rho c (T_{ig} - T_\infty)} \tag{7}$$

In these equations, k denotes the thermal conductivity of the material, ρ is the density, c is the specific heat capacity, T_{ig} represents the surface temperature at ignition, T_∞ is the ambient temperature, $\dot{q}_e^{''}$ is the external heat flux, l is the sample thickness, CHF refers to the critical heat flux.

Fig. 9 shows the relationship between the reciprocal of ignition time and external heat flux at different power-law indices (n). When n = 0.5, the fitted linear regression yields a slope of 0.00245 and an intercept of 0.00251. When n = 1, the slope and intercept are 0.00032 and 0.00427, respectively. The corresponding intersections with the horizontal axis, i.e., the critical heat fluxes (CHF), are calculated to be 0.93 kW/m^2 for n = 0.5 and 13.28 kW/m^2 for n = 1. Both fitted lines showed a coefficient of determination (R^2) exceeding 95 %, with the linear fit for n = 1 exhibiting slightly higher accuracy, which suggests better agreement with thermally-thin behavior. Since both fits were satisfactory, temperature measurements [15,17] were also introduced to further illustrate the material thermal penetration characteristics.

Considering the size and symmetry of the sample, thermocouples were placed at the center of the upper and lower surfaces (1), at one-quarter of the centerline (2), and at one-quarter of the diagonal (3) for this experiment (see Fig. 10). Fig. 11 shows the temperature variations

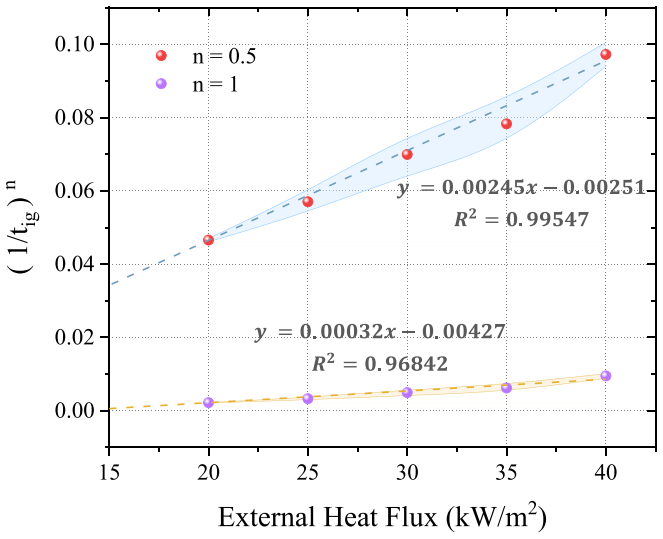

Fig. 9. Linear fit between the sample and the inverse power of ignition time.

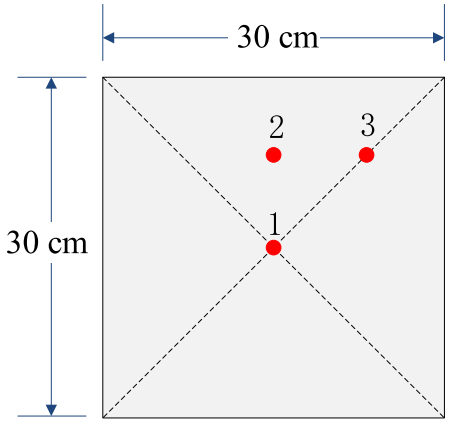

Fig. 10. Front and rear surface thermocouple distribution.

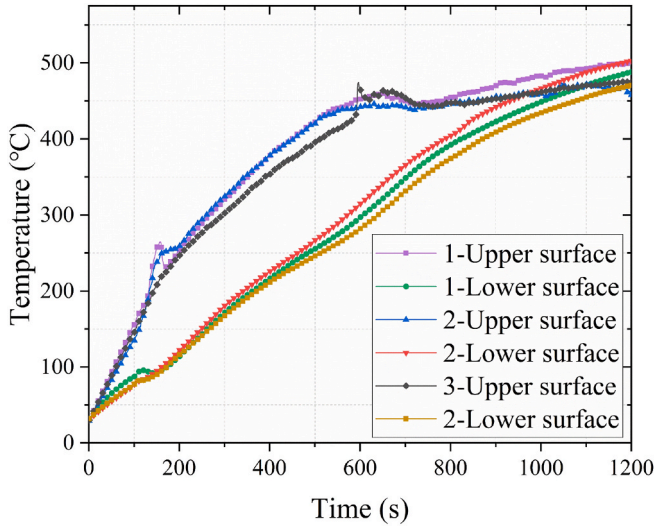

Fig. 11. Temperature evolutions collected from ignition experiments.

at each thermocouple location for 40 kW/m^2 external radiative heat flux. It is evident that the surface temperatures at different points on the same side of the sample remain relatively consistent, but the temperature difference between the two surfaces is quite significant. Before 492 s, the temperature of the upper and lower surfaces of the PV module steadily increased over time. After 492 s, a sharp rise in temperature occurred at the thermocouples located at the corners, which is attributed to the flames reaching these points during the combustion process. Prior to 492 s, the largest temperature gradient within the material occurred at 425 s, with a temperature difference of 167 °C.

Based on the presence of a significant thermal gradient, it can be concluded that the double-glass PV module used in this experiment behaves as a thermally-thick material, which provides a necessary basis for applying conduction-based thermal models to more accurately predict ignition time. However, it should be noted that, as discussed in Section 3.1, the ignition of the PV module is primarily caused by the internal PVB interlayer. Before the melting and overflow of PVB, the material primarily absorbs heat through radiation and conduction via the glass layer. After the melting and overflow occur, the heat transfer mechanism gradually transitions to predominantly conduction and convection, depending on the extent of melting. Moreover, as the PVB melts, pyrolysis transitions the material from a multi-layer composite to a single material, with its thickness changing accordingly.

3.3. Heat release rate per unit area (HRRPUA)

Heat release rate per unit area (HRRPUA) refers to the amount of heat released per unit time and per unit area during the burning of a combustible material [40]. As a critical parameter for assessing fire hazards, HRRPUA quantitatively describes the scale and growth rate of a fire.

In this study, the HRRPUA was based on Hess's Law, as shown in Equation (8) [41]:

$$\dot{q}(t) = E\left(\dot{m}^0_{O_2} - \dot{m}_{O_2} + \Delta\dot{m}^0_{O_2(co\to co_2)}\right) - \dot{q}_{co\to co_2} \tag{8}$$

In this equation, E represents the energy released per unit mass of fuel consumed by oxygen, approximately 13.1 MJ/kg [42]. $\dot{m}^0_{O_2}$ denotes the initial mass flow rate of oxygen, $\dot{m}_{O_2}$ is the measured oxygen mass flow rate $\Delta\dot{m}^0_{O_2(co\to co_2)}$ represents the CO mass flow rate at the sampling location, and $\dot{q}_{co\to co_2}$ corresponds to the heat release rate from the complete oxidation of CO.

Fig. 12 shows the transient evolution of the HRRPUA of the sample under thermal radiation. It is evident that as the external heat flux increases, the HRRPUA increases significantly as well, while the time required to reach the peak HRRPUA decreases. For heat fluxes between

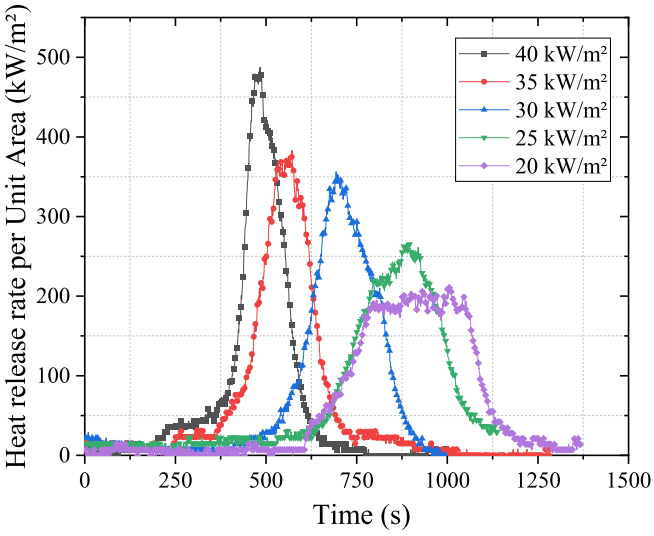

Fig. 12. HRRPUA curves of the double-glass PV Samples.

30 and 40 kW/m^2, the HRRPUA follows a typical ramp-up-and-down curve. However, for 20 kW/m^2 and 25 kW/m^2, the HRRPUA curve first increases, then stabilizes for approximately 350 s, before declining, resembling a ramp with a truncated peak.

At 20 kW/m^2, the sample took over 600 s from ignition to complete burning. At 30 kW/m^2, the material burned more rapidly but did not reach its maximum intensity, with the burn-out time around 400–500 s. At 40 kW/m^2, the combustion process was the shortest. The intense burning resulted in faster fuel consumption, with the HRRPUA rapidly decreasing after reaching its peak. The entire burning process was essentially completed within 300 s. This indicates that higher heat fluxes cause rapid fuel consumption, with combustion concentrated in a short duration. In contrast, at lower fluxes, the combustion is milder, and due to the lower intensity and slower rate, the material takes longer to burn out.

Table 3 lists the peak heat release rate per unit area (pHRRPUA), the time to reach peak HRRPUA (TTPH), the average HRRPUA growth rate (AGR), and the total heat release for the double-glass PV modules under various heat flux conditions. The pHRRPUA value shown represents the highest point among all the peaks observed. As the external heat flux increases, the maximum heat power released during combustion significantly increases, and the time required to reach the peak HRRPUA decreases. From 20 kW/m^2 to 40 kW/m^2, the pHRRPUA of the sample more than doubles.

The HRRPUA growth rate indicates how quickly HRRPUA increases at the early fire stage, calculated as the average rate from ignition to the first peak. At the lower heat flux (20 kW/m^2), ignition is slower, and the initial combustion progresses gradually, with an average growth rate of less than 3 kW/(m^2·s). At moderate heat flux (30 kW/m^2), ignition occurs faster, and the HRRPUA rise is notably accelerated. Under high heat flux, the material ignites rapidly, and HRRPUA rises sharply, with an average growth rate of 4.7 kW/m^2. The greater the external heat flux, the faster the initial growth of the combustion reaction. High radiation flux causes faster surface degradation of the material and the release of combustible gases, leading to a sharp increase in HRRPUA in a short time. Conversely, under lower fluxes, insufficient thermal feedback results in a slower HRRPUA rise.

The total heat release per unit area (THRPUA) for all five test conditions was calculated and found not to increase with the heat flux. Instead, it decreased from 81 MJ/m^2 to 71 MJ/m^2 between 25 kW/m^2 and 40 kW/m^2. This suggests that while increased radiative heat flux accelerates the combustion process, it also limits the completeness of combustion of the internal combustible materials to some extent.

Here, we introduce the fire growth index to measure the fire intensity of the double-glass PV models. It is obtained by dividing the pHRRPUA by the TTPH. This index can assess the fire performance of the material in buildings and predict the spread of the fire.

$$\mathrm{FIGRA} = \frac{\mathrm{pHRRPUA}}{\mathrm{TTPH}} \tag{9}$$

The Fire Growth Rate (FIGRA) [43] of the double-glass PV modules is shown in Fig. 13. According to previous research [15,16], the FIGRA of polymer-coated PV modules at an external heat flux of 30 kW/m^2 is 2.7, which is higher than that of the double-glass PV components. The FIGRA of cover-glass modules is 0.2, lower than that of the double-glass PV modules. Based on the fitted curve, this trend is also predicted to apply to conditions of 50 kW/m^2 and 70 kW/m^2. This indicates that, under the same radiative conditions, the fire intensity of double-glass PV modules is higher than that of cover-glass modules but lower than that of polymer-coated PV modules.

Table 3
pHRRPUA, TTPH, AGR and THR of the double-glass PV Samples.

External Heat Flux (kW/m^2)	Double glass PV			
	pHRRPUA (kW/m^2)	TTPH (s)	AGR (kW/(m^2·s))	THRPUA (MJ/m^2)
20	215	1005	0.70	81
25	265	889	0.76	81
30	356	694	1.25	76
35	383	572	1.23	73
40	487	484	1.63	71

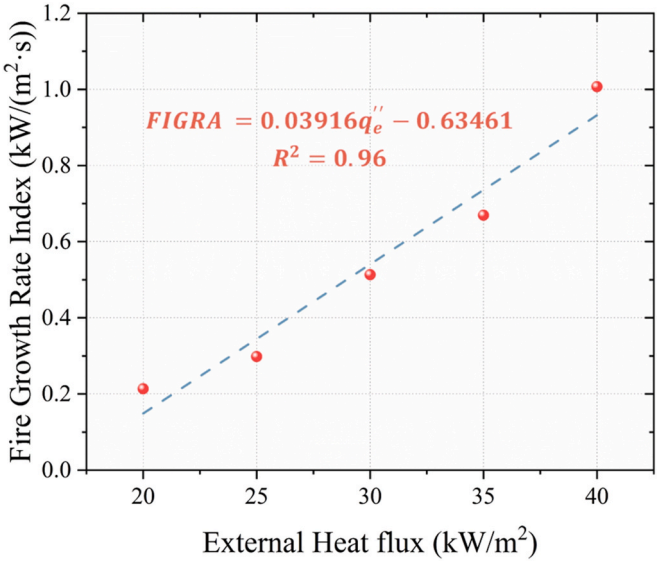

Fig. 13. Fire growth rate index of the double-glass PV modules.

3.4. Mass loss rate (MLR)

Fig. 14(a) shows the mass loss curves under varying heat flux conditions, with data measured using an electronic balance with an accuracy of 0.1 g. The general trend observed is that as heat flux increases, the amplitude of the curve's decay also increases, indicating that a greater amount of residue remains after the burning. However, this mass loss is relatively small compared to the overall mass of the PV module itself. From the start to the end of the experiment, the mass loss at the heat flux of 40 kW/m^2 was approximately 188.8 g, about 6.30 % of the total mass, while at 20 kW/m^2, the mass loss was around 164.1 g, representing about 5.47 % of the total mass. This is because the burning of double-glass PV modules primarily consumes the PVB material, while the heaviest part, the glass panel, is non-combustible.

It is critical to note that there are some abrupt mass changes marked by red circles in Fig. 14(a), which are caused by the glass fragments detaching during the breakage moment. These 'unexpected events' not only reflect the physical risks of the PV modules during combustion but also indicate that predicting the combustion time and peak HRRPUA values based solely on mass loss is not feasible.

Additionally, it was observed that at lower power levels (such as 20 kW/m^2), the mass loss occurred more slowly, and the curve was relatively flat. As the heat flux increased, the curve became progressively steeper, indicating that heat flux also affects the MLR. To visualize the changes in mass loss more clearly, the mass loss curves were differentiated to obtain the MLR of the sample, and the rates for 20, 30, and 40 kW/m^2 were plotted (Fig. 14(b)). The shapes of these MLR curves were similar, and multiple peaks were observed during the process. This can be explained in conjunction with the HRRPUA curves discussed earlier, as the combustion of double-glass PV modules occur in stages, starting from the edges and progressing toward the entire module. Therefore, the degree of mass loss at different stages varies, and the MLR before and after breakage also changes accordingly. Overall, the peak MLR values for the three curves were 1.0 g/s, 0.95 g/s, and 0.85 g/s under the heat fluxes of 20, 30, and 40 kW/m^2, respectively, gradually decreasing with

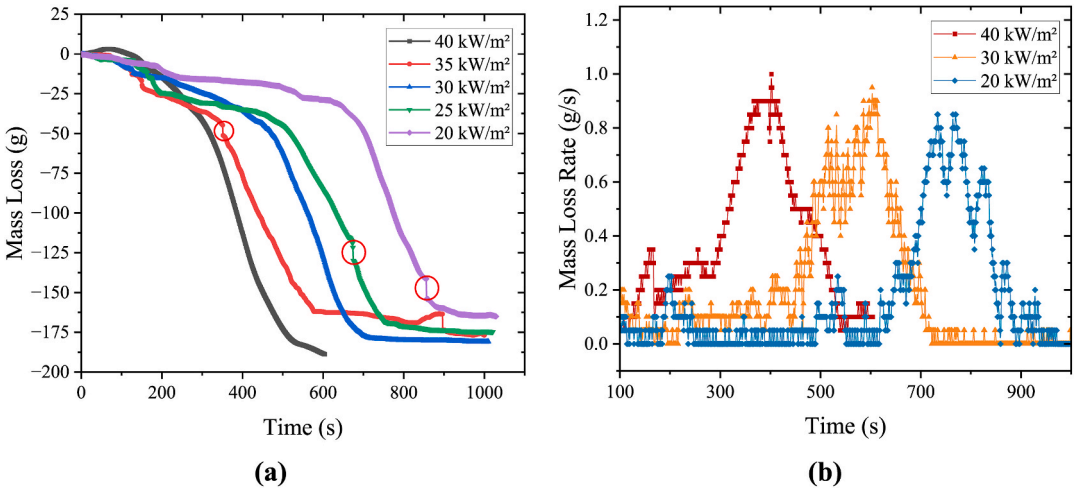

Fig. 14. (a) Mass loss curves of the double-glass PV (red circles denote abrupt mass changes caused by glass fracture); (b) MLR curves of the double-glass PV.

an increase in the heat flux. The same trend was found for the time to the peak MLR, which occurred at 402 s, 603 s, and 734 s, respectively, with an increasing heat flux.

3.5. Numerical prediction results of inner layer temperature of double-glass PV modules

To predict the temperature evolution within each layer of double-glass PV modules prior to ignition, a numerical model was developed to couple the solid heat transfer and pyrolysis kinetics of multilayer composite materials subjected to external radiative heat flux.

The proposed layer-resolved modeling framework (in Section 2.3) captures the thermal-barrier effect that arises in local regions of low conductivity and avoids the temperature-field smoothing errors commonly induced by abrupt inter-layer conductivity jumps. As a result, it faithfully reproduces the inner layer temperature profile of every material. In particular, the model resolves the temperature plateau associated with the endothermic pyrolysis of the PVB interlayer, providing a more reliable indicator for identifying phase-transition thresholds.

Fig. 15 illustrates one-dimensional temperature contours across the laminate thickness at 0–250 s under a 30 kW/m^2 external heat flux. The time-dependent distributions clearly reveal the downward propagation of heat from the irradiated top surface. At 0 s, the temperature is uniform and low throughout the stack. By 100–150 s, a pronounced gradient develops: the top surface heats rapidly, whereas the bottom layers remain relatively cool. At 200 and 250 s, the thermal wave penetrates deeper, yet a substantial temperature difference between the upper and lower surfaces persists. This stratification corroborates the one-dimensional heat-conduction assumption and confirms that solid-phase conduction governs the early-to-mid heating regime.

Fig. 16 compares measured and simulated top and bottom surface temperatures of the double-glass PV module under five external heat-flux levels. For both surfaces, the simulations accurately track the temperature rise, with discrepancies remaining below 5 %. The residual error is mainly attributable to realistic scenarios not yet represented in the model: (i) phase transitions in the polymer interlayer during pyrolysis, (ii) localized perturbations in surface heat transfer conditions and thermocouple readings caused by the evolution of pyrolysis gases, and (iii) changes in interfacial thermal contact resistance resulting from interlayer melting and morphological alteration.

The model framework is not limited to double-glass modules. By adjusting material properties, thermal conductivity, specific heat capacity, and kinetics, it can be extended to a wide range of PV architectures. Such a generalized approach offers a predictive toolbox for the PV industry, spanning material selection (assessing the thermal tolerance of encapsulation polymers), structural optimization (layer-thickness allocation and interface engineering), and smart fire safety control (triggering agent release at critical temperatures). It thus has the potential to contribute to a shift in fire protection design from empirical practices toward a prediction-driven paradigm.

3.6. Gas emission

3.6.1. Gas species

To analyze the combustion toxicity of double-glass PV modules, it is essential to consider the thermal degradation of the combustible core material. Polyvinyl Butyral (PVB) is a polymer formed by the condensation of polyvinyl alcohol and butyraldehyde [44–46] that is known for its excellent bonding properties with glass, metal, ceramics, wood, and other materials. It is also resistant to light, abrasion, and water. Its chemical molecular structure, as shown in Fig. 17, consists of carbon (C),

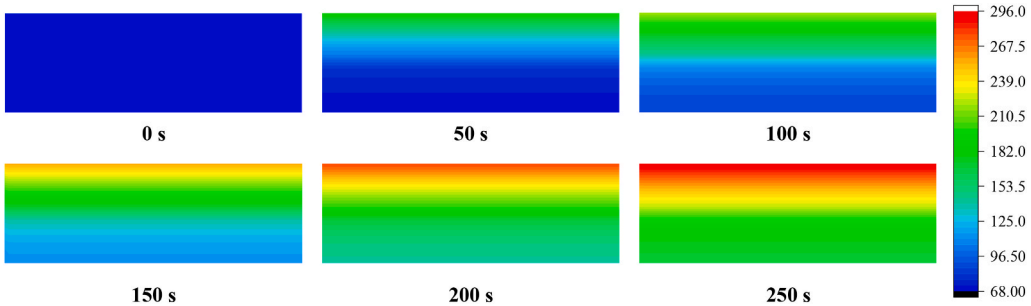

Fig. 15. Temperature distributions along the module thickness under a 30 kW/m^2 heat flux at selected times.

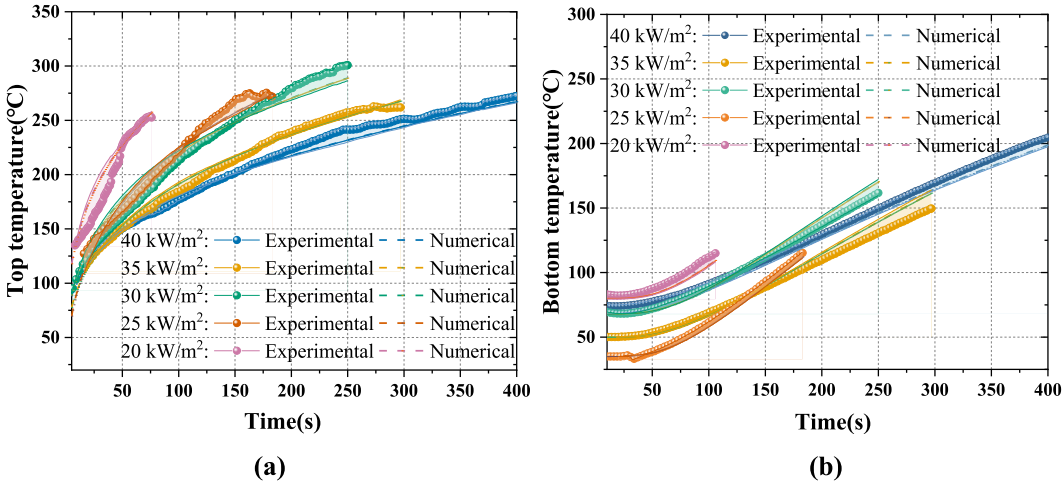

Fig. 16. Experimental vs. simulated surface temperatures of double-glass PV modules: (a) top surface. (b) bottom surface.

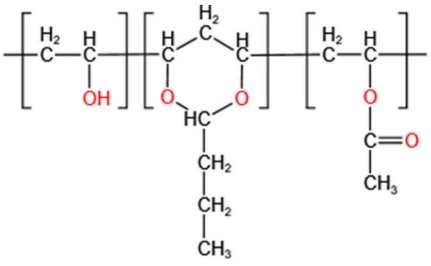

Fig. 17. PVB structural formula.

hydrogen (H), and oxygen (O) elements.

The thermal degradation behavior of PVB has been widely studied. Eldin et al. [47] investigated the characteristics of PVB-encapsulated glass and found that nearly all of characteristic functional groups of PVB are sensitive to thermal degradation. The aldehyde ring groups virtually disappear, and there is a sharp reduction in the number of hydroxyl and acetate groups. Ivanov et al. [48] studied the thermal oxidation degradation of PVB at 60–300 °C and found that the thermal oxidation degradation occurs in multiple stages, with pyrolysis promoting the formation of carbonyl and dienyl groups. Xu [45] et al. researched the thermal aging kinetics and mechanisms of PVB materials, confirming that the hydroxyl group (-OH) is an active site in the thermal aging process of PVB. In our previous studies, we also observed the deformation vibration absorption peaks of CO_2 and CO molecular bonds using TGA-FTIR. Therefore, during the analysis of gas components, we mainly focus on the gases CO_2, CO, and H_2.

The upper and lower glass panels of the sample are made from ordinary clear glass and ultra-white glass, respectively. Their primary component is SiO_2, with a mass fraction of about 72.20 %. The remaining portion contains other substances, predominantly SO_2 and Fe_2O_3. Table 4 lists the proportions of materials, excluding SiO_2, as provided by the manufacturer. The compositions of the two types of glass are nearly identical, with the most significant difference being that the iron content in the ordinary clear glass is nearly ten times that of the ultra-white glass. This difference in iron content affects their light transmission properties, making the ordinary clear float glass have a higher light transmittance than ordinary glass, without displaying the green tint typically observed in standard glass. Additionally, it is important to note that both glass types contain SO_2, which was included in the measurement range during the experiment.

Table 4
The proportions of non-SiO_2 components in ultra-white and ordinary clear glass.

Materials	The proportion of each substance (%)						
	SO_2	Na_2O	CaO	MgO	Al_2O_3	K_2O	Fe_2O_3
Ultra-white glass	0.20	13.70	9.10	3.30	1.25	0.20	0.01
Ordinary clear glass	0.20	13.70	9.10	3.30	1.25	0.20	0.10

The release of CO_2 and CO during the pyrolysis combustion process is shown in Fig. 18. At different heat fluxes, there are notable differences in the peak concentration and the timing of the CO_2 release. High heat fluxes lead to earlier and more substantial CO_2 release. For example, under the condition of 40 kW/m^2, the CO_2 concentration rapidly increases and peaks at 482 s (approximately 0.60 vol%), while at the lower heat flux of 20 kW/m^2, the peak concentration is only about 0.37 vol%, and the peak occurs later, at 815 s. As the heat flux decreases, the rise in CO_2 concentration becomes slower, the peak occurs later, and the peak concentration is lower. The initial growth rate steepens with irradiance, indicating more rapid pyrolysis and gas evolution at higher flux. Post-peak behavior is likewise flux dependent: at 40 kW/m^2, CO_2 decays to near-baseline within 400 s, whereas at 20 kW/m^2 concentrations above 0.30 vol% persist beyond 1400 s. Collectively, these data demonstrate that stronger radiative heating not only advances and amplifies the CO_2 peak but also shortens the overall emission period, reflecting faster devolatilization and subsequent oxidation of the PVB encapsulant.

The release behavior of CO is more complex and is influenced by the heat fluxes. The curve shows sharp increases and decreases, with more frequent fluctuations, indicating that CO is produced in large quantities in a short period and then quickly depleted. However, the general trend is that higher heat fluxes lead to earlier release and higher peak concentrations of CO, while at lower heat fluxes, CO release is delayed and more sustained. Under the 40 kW/m^2 condition, the maximum CO concentration recorded was 23.41 ppm, which was the highest among all test conditions, followed by a gradual decrease. In contrast, at 20 kW/m^2, CO concentration increases much more gradually, reaching its peak at 817 s and then slowly decaying, elongating the entire release process. At intermediate heat-flux levels, the CO release exhibits a moderate peak whose occurrence time falls between those observed under the lower and higher flux conditions. CO and CO_2 display similar temporal patterns: higher heat flux produces an earlier CO peak and a larger maximum concentration, whereas lower heat flux delays the peak and prolongs the emission period, even though CO can still reach appreciable levels.

The concentration of H_2 at different heat fluxes is relatively low (Fig. 19), but its release timing and rate are significantly influenced by heat fluxes. At high heat fluxes, H_2 is released rapidly: for instance, at 40 kW/m^2, the peak is reached at 482 s (approximately 1.60 ppm),

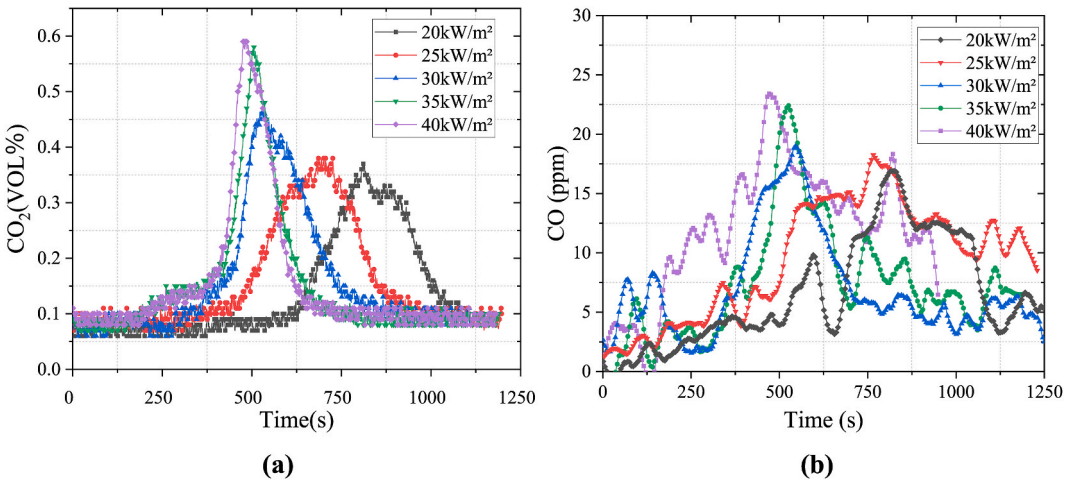

Fig. 18. (a) Carbon dioxide concentration of double-glass PV modules. (b) Carbon monoxide concentration of double-glass PV modules.

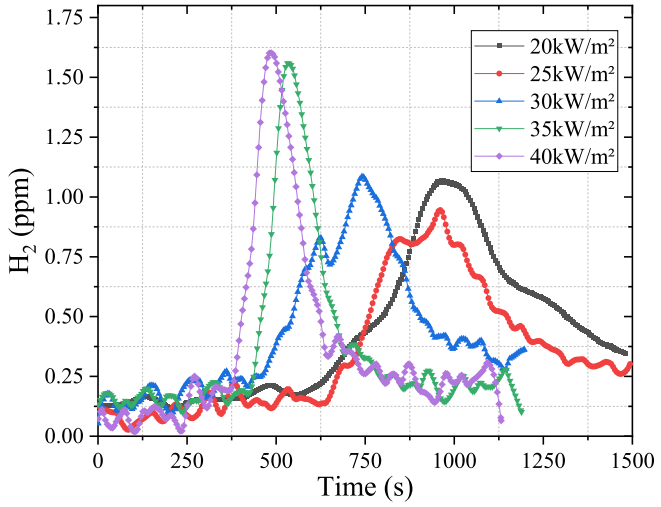

Fig. 19. The variation of hydrogen concentration of double-glass PV modules.

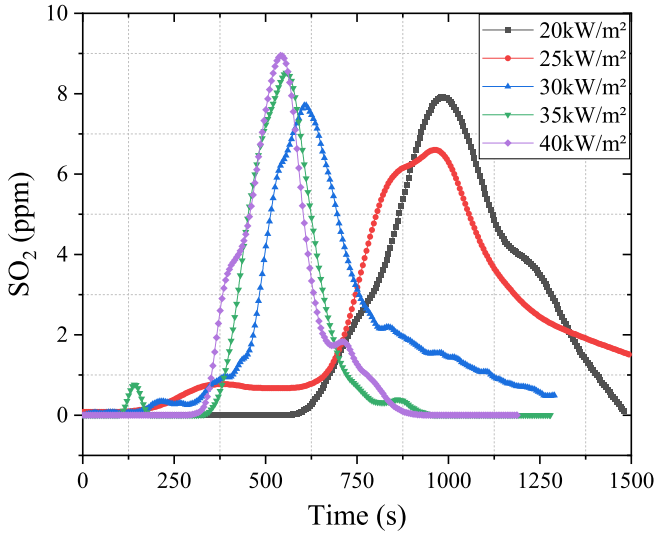

Fig. 20. The variation of sulfur dioxide concentration of double-glass PV modules.

exhibiting a sharp single peak. Reducing the heat flux density delays the release of H_2: under 20 kW/m^2, the peak occurs at 967s, reaching 1.06 ppm. Interestingly, the peak concentration of H_2 does not change monotonically with heat flux density, the highest (40 kW/m^2) and lowest (20 kW/m^2) heat flux conditions result in higher peak concentrations than at some intermediate heat fluxes. For example, at 30 kW/m^2, the peak concentration is only about 0.94 ppm, lower than the peaks at 20 and 25 kW/m^2. This suggests that at high heat flux, rapid volatilization leads to quick decomposition, producing an instantaneous high concentration of H_2, while at low heat flux, slower secondary decomposition also accumulates and releases a higher concentration of H_2.

In terms of change rate, at 40 kW/m^2, the concentration of H_2 rises and falls very rapidly, reaching the peak within a few hundred seconds and quickly dropping back to near zero. In contrast, at 20 kW/m^2, H_2 increases slowly, and after reaching the peak, the concentration decreases gradually, not returning to background levels by the end of the experiment. In summary, as heat flux density increases, the H_2 release peak occurs significantly earlier and shows a rapid, instantaneous release characteristic; however, the peak concentration does not decrease monotonically with heat flux, with lower peaks observed at intermediate heat fluxes.

The release of SO_2 is influenced not only by the composition of the glass itself but also by the additives present in the sample. Fig. 20 illustrates a distinct pattern in its release behavior corresponding to variations in heat flux density. High heat flux density promotes early and substantial SO_2 release: at 40 kW/m^2, SO_2 concentration increases rapidly and reaches its peak (8.95 ppm), then quickly drops to near zero. Lowering the heat flux density delays the release of SO_2 and changes its peak concentration: at 20 kW/m^2, the peak occurs at 980 s, with a concentration of about 7.91 ppm, close to the level observed under high heat flux conditions. At intermediate heat flux densities (25–35 kW/m^2), the peak timing and concentration fall between the two extremes. For example, at 30 kW/m^2, the peak is 7.72 ppm and occurs at approximately 614 s, while at 25 kW/m^2, the peak is about 6.61 ppm and occurs at 961 s.

It is evident that the SO_2 peak concentration does not increase monotonically with heat flux density, the highest and lowest heat flux conditions result in similar high peaks, while intermediate heat flux levels produce slightly lower peaks. Regarding the release rate, at high heat flux densities, SO_2 concentration rises steeply, reaching the peak in a short time and quickly decreasing. At lower heat flux densities, SO_2 accumulates slowly, and after the peak, the concentration remains high for a longer period, with residual SO_2 present even at the end of the experiment. Overall, higher heat flux densities cause SO_2 to be released earlier and more intensely (with an earlier peak and faster rate), while

lower heat flux densities delay SO_2 release and extend its duration.

3.6.2. Toxic threat

The toxicity of fire smoke can be calculated based on the concentration of toxic components in the combustion products and the effective exposure dose [49], as expressed in formula (10), which represents the Fractional Effective Dose (FED).

$$FED = \sum_{i=1}^{n} \int_0^t \frac{C_i}{(C \cdot t)_i} dt \tag{10}$$

Here, C_i represents the concentration of toxic component i (ppm), and $(C \cdot t)_i$ denotes the product of concentration and exposure time (ppm·min). In practical calculations, the lethal concentration (LC_{50}) can be used as the effective exposure dose, simplifying the Fractional Effective Dose (FED) to the ratio of the average concentration of toxic component i over the exposure time to its LC_{50} value, as shown in equation (11):

$$FED = \frac{C_1}{LC_{50,1}} + \frac{C_2}{LC_{50,2}} + \frac{C_3}{LC_{50,3}} \tag{11}$$

Since the test values for H_2 are only between 1 and 1.7 ppm, and it only poses an asphyxiation hazard without significant toxicity, we have neglected its presence in the calculation and only considered the values of the other three gases, as shown in the following equation:

$$FED = \frac{C_{CO_2}}{LC_{50,CO_2}} + \frac{C_{CO}}{LC_{50,CO}} + \frac{C_{SO_2}}{LC_{50,SO_2}} \tag{12}$$

The LC_{50} values used in the calculation are as follows: LC_{50,CO_2} is 20 %, $LC_{50,CO}$ is 5000 ppm, and LC_{50,SO_2} is 1400 ppm. According to the international standard ISO 13571 [50], multiple FED thresholds are typically used to assess life safety risks based on the sensitivity of different populations. A FED value of 0.30 is considered the threshold at which the most sensitive groups (such as the elderly, children, or patients) may experience disability, while FED = 1.00 represents the point at which, theoretically, 50 % of individuals can survive. The lower the FED, the weaker the gas toxicity, and the safer the environment.

The FED values obtained under different radiative heat flux conditions in this experiment are shown in Fig. 21, alongside the FED values of cover-glass PV [15] and PET-laminated PV [16] modules measured under the same heat flux conditions. The results indicate that higher heat flux accelerates thermal decomposition and combustion of PV module materials, leading to earlier emission of toxic smoke components and a rapid increase in FED. Conversely, under lower external heat flux conditions, inadequate heating delays material degradation and combustion, resulting in a slower rate of FED accumulation.

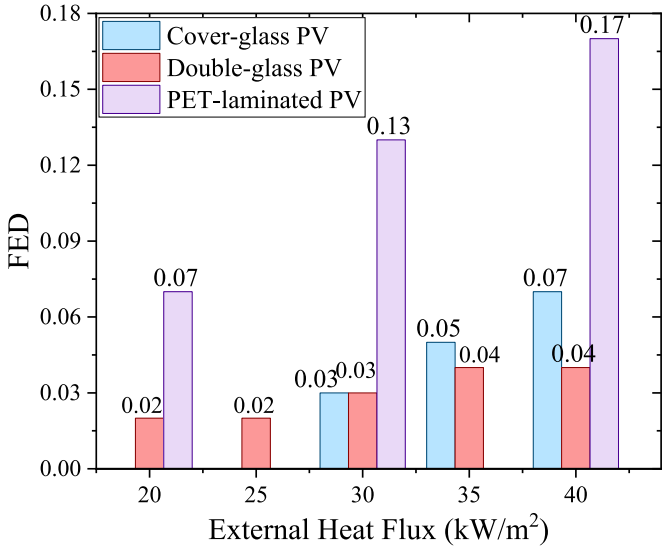

Fig. 21. FED of Three PV Configurations Subjected to the same external heat fluxes.

Comparison of FED data shows that the FED of double-glass PV modules remained low and nearly unchanged (0.02–0.04) across the tested heat flux range (20–40 kW/m^2). In contrast, cover-glass PV modules exhibited a marked increase in FED above 30 kW/m^2, while PET-laminated PV modules consistently showed the highest FED values, reaching about 4.3 times that of double-glass modules at 40 kW/m^2. These differences reflect the superior flame-retardant and insulating properties of the glass-encapsulated structure in double-glass modules, as opposed to the higher combustibility and toxic gas release from the polymer layers in cover-glass and PET-laminated modules.

The study demonstrates that under the simulated fire exposure conditions, the cumulative smoke toxicity generated by burning double-glass PV modules is insufficient to pose immediate poisoning or fatality threats. These results indicate that double-glass PV modules pose a lower risk when only one module burns in a well-ventilated environment under high heat flux. Such conditions allow more time for occupant evacuation and firefighting operations. The present analysis, however, addresses gas toxicity for a single module only. Scenarios involving confined spaces, multiple-module fires, or additional combustibles could accelerate FED accumulation and therefore require separate evaluation.

4. Conclusions and perspectives

This study investigated the pyrolysis behavior of PVB-encapsulated double-glass PV modules using the early-stage fire characteristics bench. Key fire parameters including ignition time, HRRPUA, mass loss characteristics, and evolved gas composition were systematically analyzed. A coupled thermal response and pyrolysis kinetics model was developed to simulate pre-ignition processes. The main findings are summarized as follows:

(a) Experimental results show that PVB-encapsulated double-glass PV modules display thermally-thick behavior. Under increasing radiant heat flux (20–40 kW/m^2), ignition time decreased significantly (from 462 s to 118 s), while pHRRPUA (from 215 kW/m^2 to 487 kW/m^2) and MLR (from 0.85 g/s to 1.00 g/s) showed substantial increases. These results indicate that higher heat fluxes accelerate thermal degradation and fire development.

(b) Numerical simulations using a 1D transient heat conduction model achieved excellent agreement with experimental data ($R^2 > 0.95$), accurately predicting pre-ignition thermal behavior and inner layer temperature gradients. While the model provides insights into thermal risk assessment and materials optimization, its scope is confined to pre-ignition stages. Complex phenomena during combustion, such as glass fracture and interlayer melting, are not addressed and warrant future investigation.

(c) Gas analysis revealed emissions of CO, CO_2, H_2, and SO_2 during combustion. CO_2 and CO concentrations increased markedly with higher heat fluxes (by 36 % and 44 %, respectively, between 20 and 40 kW/m^2), though toxicity risks remained limited. A critical real-world implication is the severe physical hazard posed by falling glass shards from thermal breakage to firefighters and evacuees below high-rise buildings.

Drawing on these experimental and modeling insights, engineers should optimize encapsulation and structural design to enhance fire resilience in BIPV systems. Policymakers should update standards to address system-level fire risks and glass fallout in high-rise settings. However, these conclusions are drawn from component-level tests and may not fully represent the behavior of complete façade systems, where joints, framing, and insulation can notably influence fire development.

Therefore, future work should advance toward system-level

assessment, particularly investigating fire spread mechanisms across complete façade assemblies and extending predictive models to encompass full-scale fire scenarios, while also considering real-world factors such as environmental aging. These efforts will enable comprehensive risk evaluation of integrated PV systems.

CRediT authorship contribution statement

Wanning Yu: Writing – review & editing, Writing – original draft, Resources, Methodology. **Lizhong Yang:** Supervision, Resources, Project administration. **Xinyang Wang:** Writing – review & editing, Investigation. **Dimeng Lai:** Supervision, Methodology. **Grunde Jomaas:** Writing – review & editing, Investigation. **K.M. Liew:** Supervision, Resources, Project administration. **Xiaoyu Ju:** Writing – review & editing, Supervision.

Declaration of competing interest

The authors declare that they have no known competing financial interests or personal relationships that could have appeared to influence the work reported in this paper.

Acknowledgements

This work was supported by the National Nature Science Foundation of China (52506172), the National High-Level Talent Youth Project (GG2320007006), the National Foreign Experts Program (S20240148), USTC Research Funds of the Double First-Class Initiative (YD2320002009), USTC Start Research Funding (KY2320000046& KY2320000055) and the Research Grants Council of the Hong Kong Special Administrative Region, China (Project No. 9043684, CityU 11207424). Grunde Jomaas acknowledges the financial support for the FRISSBE project within the European Union's Horizon 2020 research and innovation programme (GA 952395). The authors sincerely appreciate all the support.

Data availability

Data will be made available on request.

References

[1] Ko Y, Aram M, Zhang X, Qi DH. Fire safety of building integrated photovoltaic systems: critical review for codes and standards. Indoor Built Environ 2023;32(1):25–43. https://doi.org/10.1177/1420326x211073130.
[2] Bonomo P, Frontini F, Loonen R, Reinders A. Comprehensive review and state of play in the use of photovoltaics in buildings. Energy Build 2024;323:114737. https://doi.org/10.1016/j.enbuild.2024.114737.
[3] Nair SS. A survey report of the firefighters on fire hazards of PV fire. IEEE ICSCA; 2018. p. 1–5. https://doi.org/10.1109/ICSCAN.2018.8541219.
[4] Rusin A, Wojaczek A. Changes in the structure of the Polish energy mix in the transition period to ensure the safety and reliability of energy supplies. Energy 2023;282:128831. https://doi.org/10.1016/j.energy.2023.128831.
[5] Kristensen JS, Jacobs B, Jomaas G. Experimental study of the fire dynamics in a semi-enclosure formed by photovoltaic (PV) installations on flat roof constructions. Fire Technol 2022;58(4):2017–54. https://doi.org/10.1007/s10694-022-01228-z.
[6] Aram M, Zhang X, Qi D, Ko Y. A state-of-the-art review of fire safety of photovoltaic systems in buildings. J Clean Prod 2021;308:127239. https://doi.org/10.1016/j.jclepro.2021.127239.
[7] Hondo H. Life cycle GHG emission analysis of power generation systems: japanese case. Energy 2005;30(11–12):2042–56. https://doi.org/10.1016/j.energy.2004.07.020.
[8] Liu X, Huang Y, Shen C, Lu L. Quantitative assessment on the visual effects of photovoltaic double skin façade: towards a sustainable building prospect. Energy 2025;317:134642. https://doi.org/10.1016/j.energy.2025.134642.
[9] Sinha A, Sulas-Kern DB, Owen-Bellini M, et al. Glass/glass photovoltaic module reliability and degradation: a review. J Phys D Appl Phys 2021;54(41):413002. https://doi.org/10.1088/1361-6463/ac1462.
[10] Kyranaki N, Nivelle P, Bouguerra S, et al. Investigation of static and dynamic mechanical loads on light-weight PV modules for offshore floating applications. Eng Struct 2024;319:118760. https://doi.org/10.1016/j.engstruct.2024.118760.
[11] Hsiao P-C, Wang Z, Li Y, et al. Strategies for minimizing induced thermomechanical stress in glass–glass PV modules with half cells identified using finite element modelling. Sol Energy 2023;255:60–70. https://doi.org/10.1016/j.solener.2023.03.020.
[12] Tang Y, Song Z, Zhang C, Wang X, Ji J. Coupling ventilated semi-transparent photovoltaic windows with air-conditioning systems: electrical, thermal, and daylight performance across diverse cooling-season climates in China for varying window-to-wall ratios. Energy 2025:137167. https://doi.org/10.1016/j.energy.2025.137167.
[13] Fang P, Zhao LH, Song GH, Dong JQ, Zhao JL, Wang ZH. Fire safety assessment of building-integrated photovoltaics (BIPVs). Fire 2025;8(2):52. https://doi.org/10.3390/fire8020052.
[14] Chow CL, Han SS, Ni XM. A study on fire behaviour of combustible components of two commonly used photovoltaic panels. Fire Mater 2017;41(1):65–83. https://doi.org/10.1002/fam.2366.
[15] Yang HY, Zhou XD, Yang LZ, Zhang TL. Experimental studies on the flammability and fire hazards of photovoltaic modules. Materials 2015;8(7):4210–25. https://doi.org/10.3390/ma8074210.
[16] Ju X, Zhou X, Zhao K, Peng F, Yang L. Experimental study on fire behaviors of flexible photovoltaic panels using a cone calorimeter. J Fire Sci 2018;36(1):63–77. https://doi.org/10.1177/0734904117740855.
[17] Liao B, Yang L, Ju X, Peng Y, Gao Y. Experimental study on burning and toxicity hazards of a PET laminated photovoltaic panel. Sol Energy Mater Sol Cells 2019;206:110295. https://doi.org/10.1016/j.solmat.2019.110295.
[18] Wang Y, Wang SX, Zhao QY. Experimental investigation on the combustion performance of single-glass and double-glazed photovoltaic modules. Sol Energy Mater Sol Cells 2025;285:113528. https://doi.org/10.1016/j.solmat.2025.113528.
[19] Liao BS, Ju XY, Lai DM, Yang LZ. Experimental study of combustion characteristics of PET laminated photovoltaic panels by fire calorimetry. Sol Energy Mater Sol Cells 2023;253:112242. https://doi.org/10.1016/j.solmat.2023.112242.
[20] Xu HM, Li YZ, Shu LH, Yin HQ. Experimental study on the influence of external heat flux and air pressure on the combustion characteristics of solar panels. Fire Technol 2025;61(1):155–82. https://doi.org/10.1007/s10694-024-01608-7.
[21] Liao BS, Jiang SH, Lai DM, Yang LZ. Investigation of combustion hazards of glass photovoltaic panels with multilayer material structures in fire scenarios. Sol Energy 2025;292:113447. https://doi.org/10.1016/j.solener.2025.113447.
[22] Song YZ, Liu TS, Ye B, Li Y. Linking carbon market and electricity market for promoting the grid parity of photovoltaic electricity in China. Energy 2020;211:118924. https://doi.org/10.1016/j.energy.2020.118924.
[23] Ju XY, Zhou XD, Gong JH, et al. Impact of flat roof-integrated solar photovoltaic installation mode on building fire safety. Fire Mater 2019;43(8):936–48. https://doi.org/10.1002/fam.2755.
[24] Aram M, Zhang X, Qi DH, Ko Y. Scaling study of smoke spread from building integrated photovoltaic (BIPV) double skin facade fire for achieving sustainable buildings and cities. Sustain Cities Soc 2023;97:2210–6707. https://doi.org/10.1016/j.scs.2023.104648.
[25] Aram M, Zhang X, Reda I, Dghim M, Qi DH, Ko Y. Similarity assessment of using helium to predict smoke movement through buildings with double skin facades during building integrated photovoltaics fires. J Clean Prod 2023;405:136996. https://doi.org/10.1016/j.jclepro.2023.136996.
[26] Aram M, Zhang X, Qi DH, Ko Y. Sub-scale helium tests and numerical simulations for studying the effect of location and magnitude of BIPV double skin façade fires on the smoke spread. J Build Phys 2025;48(4):640–62. https://doi.org/10.1177/17442591241300710.
[27] Miao L, Chow CL. Investigation of burning photovoltaic panels on a double-skin facade with ejecting flame from an adjacent room fire. Indoor Built Environ 2019;28(7):938–49. https://doi.org/10.1177/1420326x18804591.
[28] Stølen R, Li T, Wingdahl T, Steen-Hansen A. Large- and small-scale fire test of a building integrated photovoltaic (BIPV) façade system. Fire Saf J 2024;144:104083. https://doi.org/10.1016/j.firesaf.2023.104083.
[29] Babrauskas V. Specimen heat fluxes for bench-scale heat release rate testing. Fire Mater 1995;19(6):243–56. https://doi.org/10.1002/fam.810190602.
[30] Yin L, Yong J, Qiu R. Combustion behaviors of cigs thin-film solar modules from cone calorimeter tests. Materials 2018;11(8):1353–70. https://doi.org/10.3390/ma11081353.
[31] Beckstead MW, Puduppakkam K, Thakre P, Yang V. Modeling of combustion and ignition of solid-propellant ingredients. Prog Energy Combust Sci 2007;33(6):497–551. https://doi.org/10.1016/j.pecs.2007.02.003.
[32] Boehringer JC, Spindler RJ. Radiant heating of semitransparent materials. AIAA J 1963;1(1):84–8. https://doi.org/10.2514/3.1475.
[33] Linan A. Radiant ignition of a reactive solid with in-depth absorption. Combust Flame 1972;18(1):85. https://doi.org/10.1016/s0010-2180(72)80229-3.
[34] Lai DM, Gong JH, Zhou XD, et al. Pyrolysis and piloted ignition of thermally thick PMMA exposed to constant thermal radiation in cross forced airflow. J Anal Appl Pyrolysis 2021;155:105042. https://doi.org/10.1016/j.jaap.2021.105042.
[35] Janssens M. A thermal model for piloted ignition of wood including variable thermophysical properties. Fire Saf Sci 1991;3(3):167–76. https://doi.org/10.3801/IAFSS.FSS.3-167.
[36] Janssens M. Piloted ignition of wood: a review. Fire Mater 1991;15(4):151–67. https://doi.org/10.1002/fam.810150402.
[37] Quintiere JG. The application of flame spread theory to predict material performance. J Res Natl Bur Stand 1988;93(1):61–70. https://doi.org/10.6028/jres.093.007.
[38] Rhodes BT, Quintiere JG. Burning rate and flame heat flux for PMMA in a cone calorimeter. Fire Saf J 1996;26(3):221–40. https://doi.org/10.1016/S0379-7112(96)00025-2.
[39] Spearpoint MJ, Quintiere JG. Predicting the piloted ignition of wood in the cone calorimeter using an integral model-effect of species, grain orientation and heat

flux. Fire Saf J 2001;36(4):391–415. https://doi.org/10.1016/S0379-7112(00)00055-2.
[40] Babrauskas V, Peacock RD. Heat release rate: the single most important variable in fire hazard. Fire Saf J 1992;18(3):255–72. https://doi.org/10.1016/0379-7112(92)90019-9.
[41] Janssens ML. Measuring rate of heat release by oxygen consumption. Fire Technol 1991;27(3):234–49. https://doi.org/10.1007/BF01038449/BFOMETRICS.
[42] Huggett C. Estimation of rate of heat release by means of oxygen consumption measurements. Fire Mater 1980;4(2):61–5. https://doi.org/10.1002/fam.810040202.
[43] Messerschmidt B, Pv Hees. Influence of delay times and response times on heat release measurements. Fire Mater 2000;24(2):121–30. https://doi.org/10.1002/1099-1018(200003/04)24:23.0.CO;2-K.
[44] Yamanaka S, Maruyama G, Ueyama T. The thermal decomposition of polyvinylbutyral/plzt, pmn dielectric powder composite. J Ceram Soc Jpn 1992;100(5):657–62. https://doi.org/10.2109/jcersj.100.657.
[45] Xu C, Liang S, Jin B, et al. Application of multi-channel in situ infrared spectroscopy: the case of PVB thermal aging. RSC Adv 2023;13(41):28371–81. https://doi.org/10.1039/d3ra03932c.
[46] Salam LA, Matthews RD, Robertson H. Pyrolysis of polyvinyl butyral (PVB) binder in thermoelectric green tapes. J Eur Ceram Soc 2000;20(9):1375–83. https://doi.org/10.1016/s0955-2219(99)00236-8.
[47] Eldin NMS, Sabaa MW. Thermal-degradation of poly(vinyl-butyral) laminated safety glass. Polym Degrad Stabil 1995;47(2):283–8. https://doi.org/10.1016/0141-3910(94)00118-r.
[48] Ivanov VB, Zavodchikova AA, Popova EI, et al. Accelerated testing of thermo-oxidative degradation of polyvinyl butyral. Thermochim Acta 2014;589:70–5. https://doi.org/10.1016/j.tca.2014.05.016.
[49] Hartzell GE, Emmons HW. The fractional effective dose model for assessment of toxic hazards in fires. Advances in Combustion Toxicology 2024;III:126–32. CRC Press.
[50] Pauluhn J. Risk assessment in combustion toxicology: should carbon dioxide be recognized as a modifier of toxicity or separate toxicological entity? Toxicol Lett 2016;262:142–52. https://doi.org/10.1016/j.toxlet.2016.09.012.
[51] Chen H, Liu N a, Fan W. Two-step Consecutive Reaction Model of Biomass Thermal Decomposition by DSC. Acta Phys-Chim Sin 2006;22(7):786–90. https://doi.org/10.1016/S1872-1508(06)60031-4.
[52] Yu WN, Zhou XD, Wang BX, Wang XY, Xu JH, Yang LZ, Ju XY. A comprehensive study on the thermal and fire performance of EVA, PMMA, and PVB polymers used in photovoltaic systems.Journal of Thermal. Analysis 2025;150(19):15087–101. https://doi.org/10.1007/s10973-025-14811-7.